Science Bulletin 64 (2019) 698–704

Contents lists available at ScienceDirect

Science Bulletin

journal homepage: www.elsevier.com/locate/scib

Article

Controlled fabrication, lasing behavior and excitonic recombination dynamics in single crystal $CH_3NH_3PbBr_3$ perovskite cuboids

Fangtao Li [a,b,1], Junfeng Lu [b,c,1], Qinglin Zhang [d,1], Dengfeng Peng [e], Zheng Yang [b,c], Qian Xu [b,c], Caofeng Pan [b,c,e,*], Anlian Pan [d,*], Tianfeng Li [f,*], Rongming Wang [a,*]

[a] Beijing Advanced Innovation Center for Materials Genome Engineering, Beijing Key Laboratory for Magneto-Photoelectrical Composite and Interface Science, School of Mathematics and Physics, University of Science and Technology Beijing, Beijing 100083, China
[b] CAS Center for Excellence in Nanoscience, Beijing Key Laboratory of Micro-nano Energy and Sensor, Beijing Institute of Nanoenergy and Nanosystems, Chinese Academy of Sciences, Beijing 100083, China
[c] School of Nanoscience and Technology, University of Chinese Academy of Sciences, Beijing 100049, China
[d] Key Laboratory for Micro-Nano Physics and Technology of Hunan Province, Key Laboratory for Micro/Nano Optoelectronic Devices of Ministry of Education, College of Materials and Engineering, Hunan University, Changsha 410082, China
[e] College of Optoelectronic Engineering, Shenzhen University, Shenzhen 518060, China
[f] School of Physics and Electronics, Henan University, Kaifeng 475004, China

ARTICLE INFO

Article history:
Received 15 January 2019
Received in revised form 27 February 2019
Accepted 28 March 2019
Available online 10 April 2019

Keywords:
Lead halide perovskite
Solvothermal method
Single crystal cuboid
Lasing
TRPL

ABSTRACT

As a direct bandgap semiconductor, organic-inorganic lead halide perovskite ($MAPbX_3$, MA = CH_3NH_3, X = Cl, Br, I) have been considered as promising materials for laser due to their excellent optoelectronic properties. The perovskite materials with 1D and 2D shapes were widely prepared and studied for Fabry-Pérot mode and whispering-gallery-mode (WGM) microcavities, but cuboid-shape is rarely reported. In this work, we successfully fabricated single crystal cuboid-shaped $MAPbBr_3$ perovskite with different morphologies, named microcuboid-$MAPbBr_3$ (M-$MAPbBr_3$) and multi-step-$MAPbBr_3$ (MS-$MAPbBr_3$), via solvothermal method. Furthermore, the as-prepared crystals' excitonic recombination lifetime under different pumping energy density was studied by time-resolved photoluminescence (TRPL). Based on controllable morphology and remarkable lasing properties, these cuboid shaped single crystal perovskite could be a promising candidate for small laser, and other optoelectronic devices.

1. Introduction

Organic-inorganic lead halide perovskites, particularly $MAPbX_3$ (M = CH_3NH_3, X = Cl, Br, I), have caught great attention for their excellent optoelectronic properties such as strong absorption coefficients, easily tunable bandgap, high carrier mobility, small exciton binding energy and unique defect properties [1–5]. These characteristics have boosted rapid progress in solar cell efficiency, which has been improved dramatically from 3.8% to over 23.7% in recent years [6–11]. Due to the facile solution processing, high quantum yield and tunable wavelength, lead halide perovskites also have potential for flexible and low-cost optoelectronic devices, such as laser devices, light-emission diodes (LED), and photodetectors, etc [12–15].

In recent years, considerable efforts have been devoted to synthesis of various perovskite materials, such as nanoplatelets [16–18], nanowires [12,19], quantum dots [20–22], and large single crystal bulks for the applications in various fields [23,24]. Since Deschler et al. [25] first accomplished the trihalide perovskite laser by constructing a surface-emitting vertical Fabry-Pérot cavity consisting distributed Bragg reflector (DBR) mirrors, a lot of novel perovskite lasers made by thin films and large-dimension single crystals have been reported [25–29]. Compared with the polycrystal films, single crystal possesses much lower defect density and much less grain boundaries, which will lead to superior optoelectronic performances. After the first single crystal perovskite nanolaser was realized by Xiong's group, a lot of research efforts have been devoted to develop high-performance perovskite nanolaser [18,30–32]. Zhu et al. [12] prepared the single crystal $MAPbX_3$ (X = Cl, Br, I) perovskite nanowires by solution process, and obtained high-performance Fabry-Pérot mode perovskite laser with lasing thresholds as low as ~220 nJ/cm^2 and high quality factor of 3,600. And then, Zhao et al. [33] controllably fabricated $MAPbBr_3$ perovskite microwires and microplates by selectively binding two surfactants octadecylammonium bromide (OTDB) and dodecylammonium bromide (DODB) to different crystal

* Corresponding authors.
E-mail addresses: cfpan@binn.cas.cn (C. Pan), Anlian.pan@hnu.edu.cn (A. Pan), litianfeng@henu.edu.cn (T. Li), rmwang@ustb.edu.cn (R. Wang).
[1] These authors contributed equally to this work.

https://doi.org/10.1016/j.scib.2019.04.016
2095-9273/

planes. Pan's group [34] successfully prepared single-crystal $CsPbX_3$ (X = Cl, Br, I) perovskite micro/nanorods with triangular cross section through chemical vapor deposition (CVD), the micro/-nanorods exhibited excellent laser properties with low lasing thresholds of 14.1 μJ/cm^2 and high quality factor of 3,500. In a word, one-dimensional (1D) and two-dimensional (2D) lead halide perovskite were widely prepared and studied due to the outstanding laser properties such as threshold, tunable wavelength, which are even better than traditional II-VI/III-V semiconductors. However, the mechanism of the excitonic recombination rate under different pumping energy density is still unclear. And the excitonic recombination dynamic process of $MAPbBr_3$ perovskite with different cuboid morphology prepared by the solvothermal method under different pumping energy is rarely reported.

Herein, we successfully fabricated single crystal cuboid shaped $MAPbBr_3$ perovskite via solvothermal method. By adjusting reaction time, we can control etching process and achieved M- and MS-$MAPbBr_3$ perovskite, respectively. Moreover, the high-quality, good stability, smooth surface, as well as uniform geometries enabled the as-prepared crystals to function as good microcavity for laser. Therefore, we evaluated the lasing behavior and excitonic recombination dynamics in M- and MS-$MAPbBr_3$ perovskite, and found that the as-prepared $MAPbBr_3$ perovskites exhibited favourable lasing properties. So, the cuboid shaped $MAPbBr_3$ perovskites prepared by the typical solvothermal method would be potentially applied in small laser and optoelectronic devices.

2. Experimental

2.1. Sample preparation

The MS-$MAPbBr_3$ was prepared by a typical solvothermal process. A 60 mg $(Pb(OAc)_2{\cdot}3H_2O$ was completely dissolved in 4 mL of hydrobromic acid by ultrasonic treatment for 15 min, and then 30 mL of isopropanol was added and stirred for 30 min. And then, 1.2 mL methylamine solution was rapidly injected into the above solution, and transferred into Teflon-lined autoclave, which was sealed and kept at 120 °C for 12 h in a furnace, and cooled down to room temperature. Finally, the orange product was obtained by vacuum filtration and washed with isopropanol, and then dried in a vacuum oven at 50 °C for overnight.

2.2. Characterization and measurement

The morphology and energy-dispersive X-ray spectroscopy (EDS) mapping of the $MAPbBr_3$ were collected by a field-emission scanning electron microscopy (FESEM, Hitachi SU-8020) equipped with an energy dispersive X-ray analysis system (EDX, Materials Analysis Division, Apollo XLT2). The X-ray diffraction (XRD) patterns were measured by X-ray diffractometer (PANalytical X'Pert 3 Powder) with a Cu Kα radiation (λ = 1.54050 Å) operated in the 2θ range from 10° to 50° by using the $MAPbBr_3$ powder. Transmission electron microscopy (TEM) and selected area electron diffraction (SAED) were performed on a JEM-2200FS electron microscope operating at 200 kV. Ultraviolet and visible absorption (UV–vis) spectra were recorded with a spectrophotometer (Shimadzu UV-3600). All the PL, lasing, and TRPL were performed with the confocal μ-PL system (WITec, alpha-300). The CW lasers at 400 nm were used as the excitation sources for PL measurements of the M- and MS-$MAPbBr_3$ perovskite. The laser was introduced to the confocal system and focused onto the samples through a 100× objective at the top of the samples. The PL signals of each M- and MS-$MAPbBr_3$ perovskite crystal were collected by the same objective and detected by a CCD spectrometer (600 g/mm grating). Spectra physics Ti: sapphire laser at 405 nm (100 fs, 1 kHz) was used for lasing and TRPL measurements. The pumping source was focused obliquely on the sample by a lens. The TRPL of the M- and MS-$MAPbBr_3$ perovskite was detected with a streak camera system (Hamamatsu, C10910) with a temporal resolution of about 18 ps.

3. Results and discussion

The samples were prepared by a typical solvothermal process under the reaction temperature of 120 °C. Fig. 1a–d schematically illustrated the $MAPbBr_3$ perovskite's morphology evolution from microparticles to MS-$MAPbBr_3$. At the initial stage, $MAPbBr_3$ rapidly nucleated in the precursor solution and grown to microparticles when reaction was maintained for 30 min. Then the $MAPbBr_3$ microparticles grown to M-$MAPbBr_3$ when reaction sustained about 2 h. Interestingly, as the reaction continued, the centers of lateral surfaces were etched and formed multi-steps after the reaction time lasting about 8 h. The scanning electron microscope (SEM) images in Fig. 1e–h demonstrated the morphological evolution of the $MAPbBr_3$ perovskite with the increasing of reaction time. Fig. 1e showed the morphology of $MAPbBr_3$ perovskite microparticles with cuboid shape and size in the range of 0.5–2 μm. In general, the $MAPbBr_3$ perovskite was preferentially grown to symmetrically cuboid crystal morphology due to the typical cuboid unit cell structure with high symmetry in three dimensions. As the crystal growth process predicted by Bravais-Friedel-Donnay-Harker (BFDH) law [35], when reaction time increased to 2 h, the $MAPbBr_3$ perovskite microparticles have grown into ~10 μm with flat surfaces as shown in Fig. 1f. When the reaction

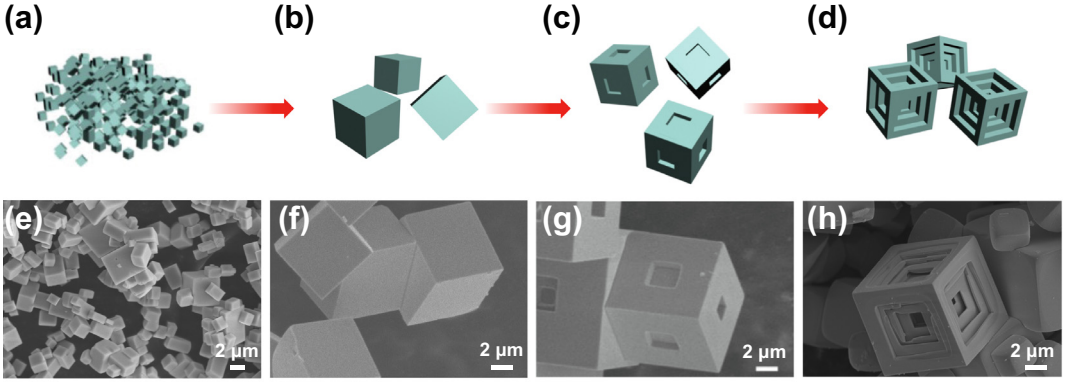

Fig. 1. (Color online) Crystal growth process and morphology of $MAPbBr_3$ perovskite. (a–d) Schematic demonstrates the morphology evolution of $MAPbBr_3$ perovskite under different reaction time. SEM images of (e) $MAPbBr_3$ nanoparticles, (f) M-, (g) SS-, and (h) MS-$MAPbBr_3$ perovskite, respectively.

time was increased to 4 h, it could be clearly observed that small etching traces formed a step on (0 0 1) surfaces as shown in Fig. 1g. Then, as the reaction proceeded further, the multi-steps emerged as shown in Fig. 1h. The lower magnification SEM images (Fig. S1 online) of the M- and MS-$MAPbBr_3$ demonstrated that the as-prepared sample still keeped uniform cuboid shape. In order to explore the effect of growth temperature on the morphology of $MAPbBr_3$ perovskite, we prepared the sample at 80, 100, 120 and 140 °C for 12 h, the SEM images were shown in Fig. S2 (online). It can be seen that the sizes of $MAPbBr_3$ microcuboid have grown from 0.5 to 2.5 to 5.0–15.0 μm when the reaction temperature increased from 80 to 100 °C. When the reaction temperature increased to 120 °C, the sample has grown to 10.0–30.0 μm and the lateral surfaces were etched and formed in multi-step-$MAPbBr_3$ perovskite. With the temperature further increased to 140 °C, the reaction proceeded more quickly and led multi-step-$MAPbBr_3$ perovskite nonuniform in size and shape. These results indicated that the reaction time and temperature play a significant impact on the synthesis of MS-$MAPbBr_3$ perovskite. The growth mechanism of the MS-$MAPbBr_3$ can be explained as follow. Due to the reaction temperature (120.0 °C) above the phase transition temperature (−36.2 °C), the $MAPbBr_3$ perovskite belonged to cuboid phase and exhibited high symmetry in three dimensions. In this crystal structure, the hydrogen bonding interactions between organic and inorganic components and strong ionic and covalent interactions within the metal halide sheets determined the crystal stability. The high reaction temperature will lead the lattice constants (a, c) increased and weakened the hydrogen bond. Furthermore, with the reaction going on, the amount of perovskite precursors would decrease and lead to dissolution of as-grown crystals. Compare with the corners and edges, lateral surfaces possessed more defects and more reactive sites. So the dissolution occurred in the lateral surface, instead of the corners and edges with higher stability [36]. Meanwhile, Ostwald ripening mechanism exists in the whole experimental process, which facilitates the initial small particles easy fusion between the center and the edge that have aligned in the same crystallographic direction. Therefore, the dissolution is a dynamic balance process of dissolution and recrystallization. Notably, the as-synthesized crystals remained the cuboid shape and flat surface, which provides the possibility for laser behavior.

Fig. 2a showed the schematic of the unit cell and crystalline structure of $CH_3NH_3PbBr_3$ perovskite, presenting that $(PbBr_6)^{4-}$ octahedrons form the framework with $CH_3NH_3^+$ located at the eight vertices of a cube. The crystalline information of as-prepared MS-$MAPbBr_3$ perovskite was investigated by TEM and XRD. Fig. 2b showed a typical low-magnification TEM image of the as-prepared MS-$MAPbBr_3$ perovskite, indicating the square shape and straight boundary. The inset showed the SAED pattern of the MS-$MAPbBr_3$, the sharp diffraction spots are ascribed to the [0 1 0] and [1 0 0] of cuboid $MAPbBr_3$ perovskite structure. In addition, the XRD pattern of MS-$MAPbBr_3$ was shown in Fig. 2c. The sharp diffraction peaks indicated the as-prepared MS-$MAPbBr_3$ perovskite possessed high quality crystalline structure. The sharp peaks appeared at the 2θ of 14.90°, 21.13°, 30.10°, 33.73°, 37.10°, 43.10°, and 48.45° corresponding to the (1 0 0), (1 1 0), (2 0 0), (2 1 0), (2 1 1), (2 2 0), (3 0 0), and (3 1 0) planes, respectively. The results were well in agreement with the crystal structure of cuboid-$MAPbBr_3$ perovskite with lattice constant a = 5.9 Å and space group of *Pm3m* as previously reported [37]. The EDS

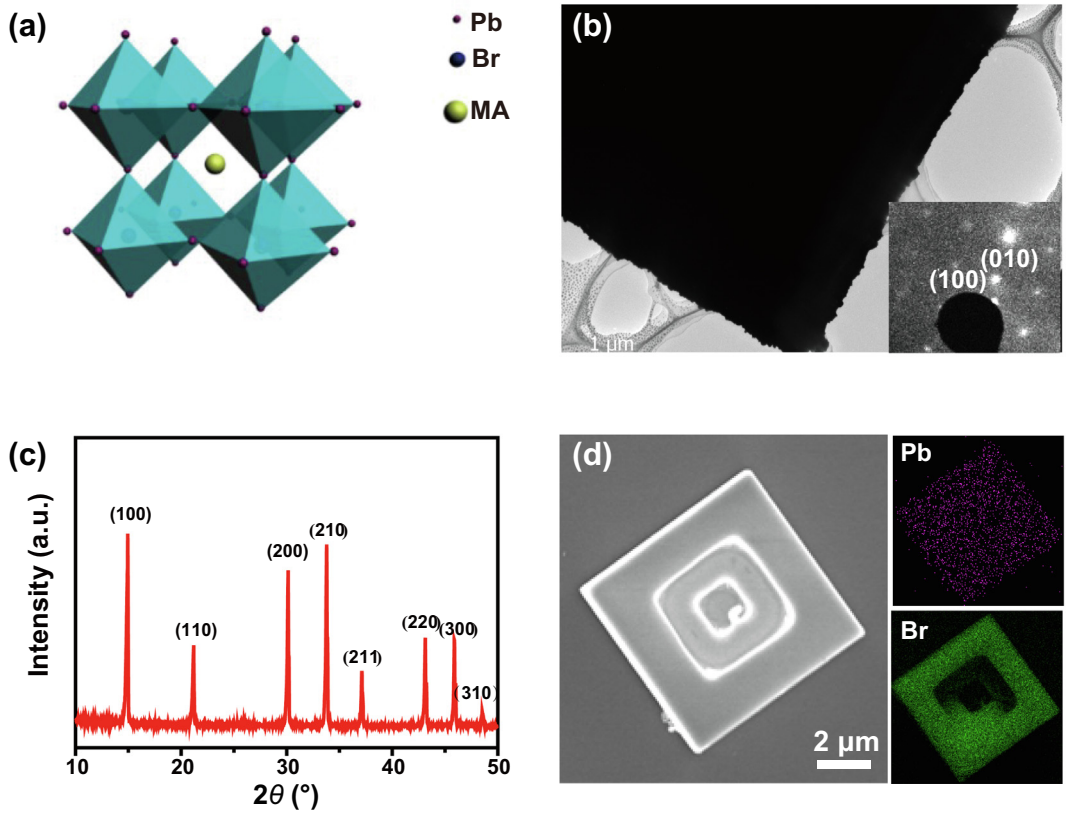

Fig. 2. (Color online) Characterization of $MAPbBr_3$ perovskite. (a) Crystalline structure of the perovskite $MAPbBr_3$. (b) TEM image of the MS-$MAPbBr_3$ perovskite. Inset: SAED pattern of $MAPbBr_3$ MS-$MAPbBr_3$ perovskite. (c) XRD patterns perovskite MS-$MAPbBr_3$ perovskite. (d) EDX mapping of the corresponding MS-$MAPbBr_3$ shows spatial distribution of Pb, Br elements.

mapping analysis of a single MS-$MAPbBr_3$ in Fig. 2d revealed that Pb and Br elements were uniformly distributed in a whole MS-$MAPbBr_3$ perovskite.

To further demonstrate the lasing behavior and excitonic recombination dynamics in M- and MS-$MAPbBr_3$ perovskite, the emission spectra with different pumping energy density were systematically investigated by the confocal μ-PL systems as shown in Fig. 3a (Witec alpha-300). The femtosecond laser beam (405 nm, 100 fs, 1 kHz) was focused (spot size, ~50 μm) by a lens, which broadly illuminated the whole individual $MAPbBr_3$ perovskite. The local optical signal at the $MAPbBr_3$ perovskite corner was collected by a confocal microscope and then detected by a CCD spectrometer. Fig. 3b showed typical UV–vis absorption and PL spectrum of the MS-$MAPbBr_3$ perovskite. It could be observed that the UV–vis absorption spectra displayed a maximum at 539.0 nm and the PL spectrum presented a single Gaussian-shape peak at 557.0 nm, in good agreement with those of $MAPbBr_3$ bulks. The PL spectra showed a narrow linewidth with a full-width at half-maximum (FWHM) of ~23.0 nm. It was worth to note that PL spectra occurred red-shift comparing with UV–vis absorption, which can be ascribed to Stokes shift. In large perovskite crystals, the bulk effect will influence on excitonic behavior, and lead to the red shift of PL peak [5,38,39]. Fig. 3c showed typical PL spectrum of single MS-$MAPbBr_3$ perovskite with side length of 17.7 μm under different pump energy density. At the pumping energy density of 197.5 μJ/cm^2, the MS-$MAPbBr_3$ perovskite showed a broad emission spectrum around the 555.0 nm with FWHM of ~26.0 nm [40]. When the pumping energy density increased to 445.9 μJ/cm^2, there were several sharp peaks near 555.0 nm and the FWHM decreased to 0.71 nm, which indicated the occurrence of laser behaviour. The quality factor Q can be calculated by the equation $Q = \frac{\lambda}{\delta\lambda}$, where the $\delta\lambda$ is the FWHM of the lasing wavelength. So the Q factor of MS-$MAPbBr_3$ perovskite corresponded to ~780. It should be noted that a slightly blue-shift of lasing peaks could be observed with the increasing of the pumping energy density. This could be owing to multiple mechanisms, such as thermally induced bandgap/refractive index change, band filling, optical density fluctuations, and electron/hole many-body interactions [12,41,42]. The insets of Fig. 3c were the dark-field optical images at low (top) and high (bottom) pump energy density. It can be seen that under low pump energy density MS-$MAPbBr_3$ perovskite showed uniform emission from the entire cuboid, when pump energy density increased above the threshold (P_{Th}), strong green lasing was emitted at the edges. This is a typical feature of an optical waveguide inside the MS-$MAPbBr_3$ perovskite, showing this construction provided a natural optical microcavity for the lasing [43]. The resonant cavity can be consider as the edges of MS-$MAPbBr_3$ perovskite. According to the previous reports, the free spectral range (FSR) of Fabry-Perot cavity was calculated by the equation: $FSR = \frac{\lambda^2}{2Ln_g}$, where λ is emission wavelength, L is the length of microcavity and n_g is the group refractive index as a function of wavelength. The n_g around 555.0 nm can be identified with a value of 6.7 and the length of edges is 17.7 μm [33]. Based on the above conditions, we obtained the FSR is 1.3 nm, and the results are consistent with the experimental results. So the optical mode of MS-$MAPbBr_3$ perovskite can be consider as Fabry-Perot mode. The peak centered at 555.2 nm may originate from the resonance of a smaller cavity, where the frame of the multilayer structure acts as an oscillating mirror. Because of the large enough FSR, only one mode was observed. Fig. 3d showed the integrated PL intensity and the FWHM of PL peak as a function of pumping energy density. When pumping energy density is under the lasing threshold (P_{Th} = 409.8 μJ/cm^2) of the MS-$MAPbBr_3$ perovskite, a broad emission spectra at the center of ~555.0 nm with a FWHM of ~26.0 nm were observed, and the integrated emission intensity increased slowly with pumping energy density, while the pumping energy density further increased above the threshold, the emission intensity increased dramatically, indicating the occurrence of lasing [12].

Similarly, the perovskite emission spectra of M-$MAPbBr_3$ perovskite with the different pumping energy density were also

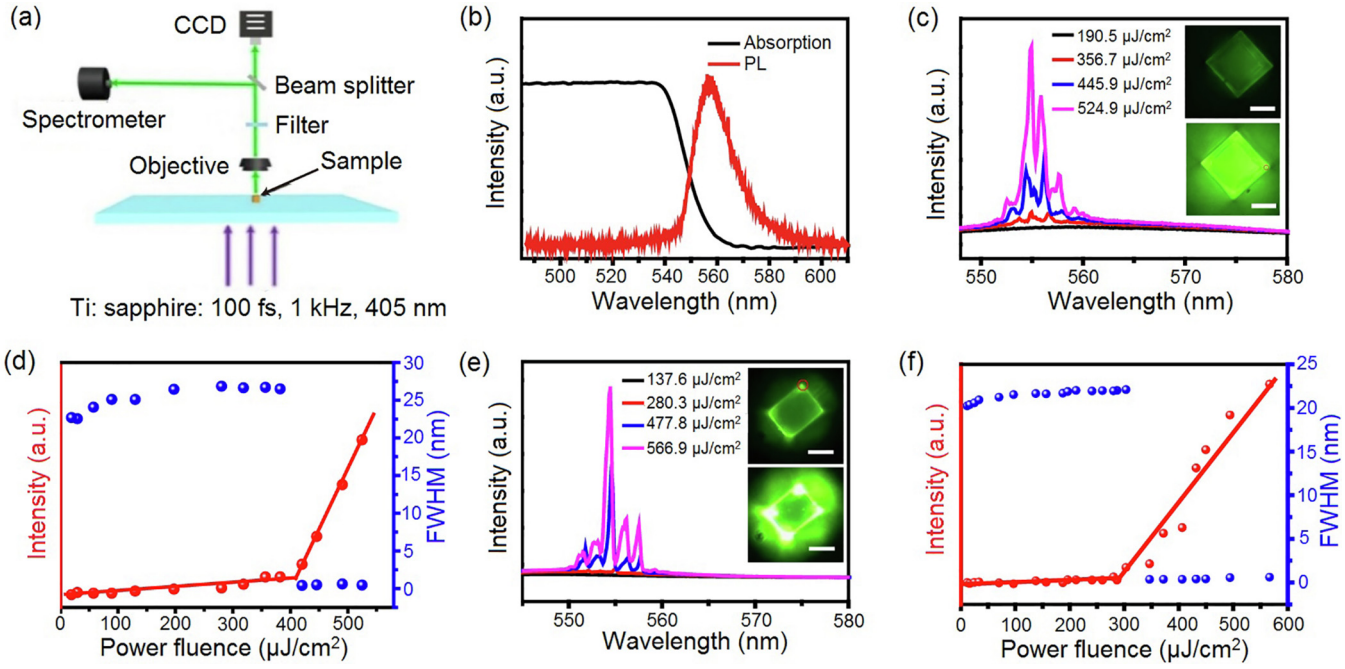

Fig. 3. (Color online) Lasing characterization of M- and MS- $MAPbBr_3$ perovskite. (a) Schematic of the lasing measurements based on single perovskite $MAPbBr_3$. (b) Absorption and PL of MS-$MAPbBr_3$ perovskite. (c) Emission spectra of MS-$MAPbBr_3$ perovskite at different pump energy density. Inset: dark-field optical images of MS-$MAPbBr_3$ perovskite. Scale bar is 5 μm. (d) Integrated intensity and FWHM of PL as a function of P_{Pump} showing the lasing threshold at 409.8 μJ/cm^2. (e) Emission spectra of M-$MAPbBr_3$ perovskite at different pumping energy density. Inset: dark-field optical images of M-$MAPbBr_3$ perovskite. Scale bar is 5 μm. (f) Integrated PL intensity and FWHM as a function of P_{Pump} showing the lasing threshold at 290.7 μJ/cm^2.

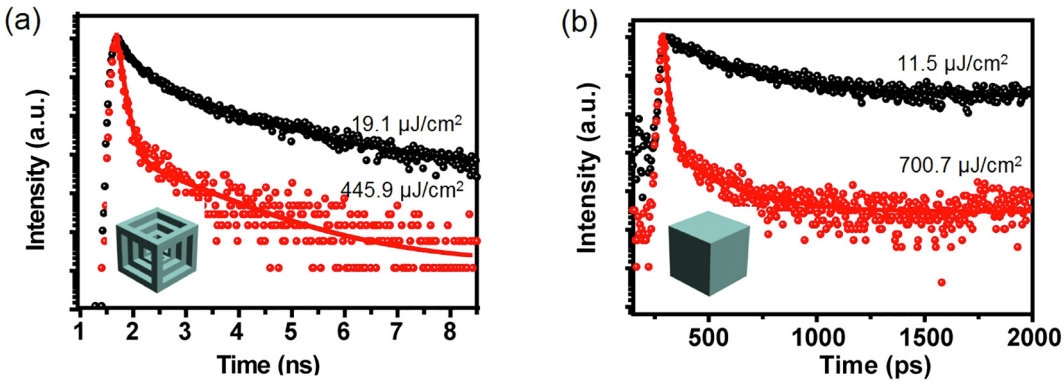

Fig. 4. (Color online) Typical TRPL decay kinetics after photoexcitation with different pumping energy density for (a) MS-and (b) M-perovskite, respectively.

measured under the same condition. Fig. 3e showed typical power-dependent PL spectrum of single M-$MAPbBr_3$ perovskite. At low pumping energy density ($P < P_{Th}$), the emission spectrum showed a broad peak around ~548.0 nm with a FWHM of ~22.0 nm, which corresponded to spontaneous emission (SPE). When the P_{Pump} was over P_{Th}, some sharp peaks appeared at 555.0 nm, indicating the occurrence of lasing action. The FWHM of the M-$MAPbBr_3$ perovskite under the pumping energy density of 477.8 μJ/cm^2 was 0.47 nm, and corresponding Q factor was 1,180 which was higher than MS-$MAPbBr_3$ perovskite's ~780. The insets in Fig. 3e were dark-field optical images at low (top) and high (bottom) pump energy density. It showed that bright green light emitted at the square cavity edges and corners, which indicated that the square surface can effectively confine the optical field and provide a perfect constructure for WGM mode cavity. The FSR of the WGM cavity can be calculated by the equation: $FSR = \frac{\lambda^2}{2\sqrt{2}Ln_g}$, where λ is the emission wavelength, L is the cavity width and n_g is the group refractive index. For WGM mode the n_g around 555.0 nm can be identified as a value of 7.1 [33]. The FSR of M-$MAPbBr_3$ perovskite is 1.5 nm, which is consistent with the experimental results. Furthermore, FDTD simulation of electric field distribution inside the M-$MAPbBr_3$ perovskite cavity as shown in Fig. S4b (online). The pattern shows typical features of WGM modes with strongest out-coupling or leakage in four corners compared with the other places. So the optical mode of M-$MAPbBr_3$ perovskite can be ascribed to the WGM mode. Fig. 3f showed the integrated intensity and the FWHM of PL as a function of P_{Pump}, which indicated lasing oscillation and gave a lasing threshold of P_{Th} = 290.7 μJ/cm^2 and lower than MS-$MAPbBr_3$ perovskite's 409.8 μJ/cm^2.

To further understand the occurrence of the lasing and excitonic recombination dynamics in M- and MS-$MAPbBr_3$ perovskite, we carried out TRPL measurements using a streak camera system with a 405 nm fs-laser as an excitation light source. The decay lifetime is derived from the biexponential decay function

$$y = A_1 \exp\left(-\frac{t}{\tau_1}\right) + A_2 \exp\left(-\frac{t}{\tau_2}\right), \quad (1)$$

where A_1 and A_2 represent the weighting factors. τ_1 and τ_2 represent the lifetime of electron-hole radiative recombination originated from different energy level.

The fitted results corresponding to the right table, and all the fitted errors were ≤2%. Fig. 4a showed the plots of the decay curves for MS-$MAPbBr_3$ perovskite, indicating the evolution from spontaneous emission (SE) to lasing emission with increasing of pumping energy density. The emission lifetime consists of two components: a short time τ_1 indicating that the emission state originated from bandedge radiative recombination and longer lifetime τ_2 denoting trap state recombination, respectively [44,45]. The averaged lifetime($\tau_{averaged}$) can be used to evaluate the competition of two mechanisms, and could be calculated according to the following equation

$$\tau_{averaged} = \frac{A_1 \times \tau_1^2 + A_2 \times \tau_2^2}{A_1 \times \tau_1 + A_2 \times \tau_2}. \quad (2)$$

It is clearly that the $\tau_{Average}$ decreased from 372.3 to 14 ps when P_{Pump} increased from 19.1 μJ/cm^2 ($P_{Pump} < P_{Th}$) to 445.9 μJ/cm^2 ($P_{Pump} > P_{Th}$), it can be ascribed to the faster recombination rate and occurrence of an effective stimulated emission process. It was also found in M-$MAPbBr_3$ perovskite as shown in Fig. 4b. For the pumping energy density below the threshold (15.5 μJ/cm^2), the $\tau_{Average}$ is 215.5 ps which shorter than MS-$MAPbBr_3$ perovskite's 372.3 ps. For the pumping energy density above the threshold (700.7 μJ/cm^2), a short emission lifetime of $\tau_{Average}$ = 16 - ps is observed, which further demonstrates the transition from spontaneous emission to stimulated emission. These TRPL results of the different cuboid shaped $MAPbBr_3$ perovskite exhibited the same feature. When pumping energy density below the lasing threshold ($P_{Pump} < P_{Th}$), the samples have longer lifetime, while the pumping energy density above the lasing threshold ($P_{Pump} > P_{Th}$), the life time decreased rapidly. It could be explained that the material undergoes spontaneous emission at low pumping energy density which means the low probability of exciton recombination, resulting in the slow lifetime. However, as pumping energy density increased to lasing threshold ($P_{Pump} > P_{Th}$), the high carrier density permitted population inversion and produced stimulated emission. Meanwhile, the high probability of exciton recombination created fast lifetime [45,46].

4. Conclusion

In summary, we successfully fabricated single crystal cuboid shaped M- and MS-$MAPbBr_3$ perovskite via solvothermal method. And the morphologies of $MAPbBr_3$ perovskite could be controllably tailored only by adjusting reaction time and temperature without any surfactant. The as-prepared crystals showed high quality, good stability, smooth surface, as well as uniform geometries. Furthermore, we achieved room-temperature optically pumped lasing in single crystal M- and MS-$MAPbBr_3$ perovskite. And the TRPL results revealed the transition from spontaneous emission to stimulated emission with the pumping energy density increasing from below lasing threshold to above lasing threshold. The lifetime of M- (MS-) $MAPbBr_3$ perovskite varied from 215.5 (372.3) ps to 16 (14) ps with increasing of pumping power density, respectively. Therefore, we believe that these single crystal cuboid shaped $MAPbBr_3$ shall shed light on the practical applications of lead halide perovskite-based optoelectronic devices.

Conflict of interest

The authors declare that they have no conflict of interest.

Acknowledgments

This work was supported by the National Natural Science Foundation of China (11674023, 51331002, 51622205, 61675027, 61505010, 51502018, 51525202 and 51432005), 111 Project (B170003), the National Key Research and Development Program of China (2016YFA0202703), Beijing Natural Science Foundation (4181004 and 4182080), and the "Thousand Talents" Program of China for Pioneering Researchers and Innovative Teams (U1404619).

Author contributions

R. Wang, C. Pan, T. Li and A. Pan designed and supervised the work. F. Li carried out the TEM measurements and performed the data analysis. D. Peng prepared the $MAPbBr_3$ perovskite sample. Q. Zhang performed the laser measurements. Z. Yang and Q. Xu performed the absorption, SEM and XRD measurements. F. Li and J. Lu wrote the manuscript. All authors read and commented on the manuscript.

Appendix A. Supplementary material

Supplementary data to this article can be found online at https://doi.org/10.1016/j.scib.2019.04.016.

References

[1] Zhang W, Saliba M, Moore DT, et al. Ultrasmooth organic-inorganic perovskite thin-film formation and crystallization for efficient planar heterojunction solar cells. Nat Commun 2015;6:6142–52.
[2] Sutherland BR, Sargent EH. Perovskite photonic sources. Nat Photon 2016;10:295–302.
[3] Eperon GE, Stranks SD, Menelaou C, et al. Formamidinium lead trihalide: a broadly tunable perovskite for efficient planar heterojunction solar cells. Energy Environ Sci 2014;7:982–8.
[4] Samuel D, Giles E, Giulia G, et al. Electron-hole diffusion lengths exceeding 1 μm in an organometal trihalide perovskite absorber. Science 2013;342:341–4.
[5] Dong S, Valerio A, Riccardo C, et al. Low trap-state density and long carrier diffusion in organolead trihalide perovskite single crystals. Science 2013;347:519–22.
[6] Kim H, Lim KG, Lee TW. Planar heterojunction organometal halide perovskite solar cells: roles of interfacial layers. Energy Environ Sci 2016;9:12–30.
[7] Shao Y, Fang Y, Li T, et al. Grain boundary dominated ion migration in polycrystalline organic-inorganic halide perovskite films. Energy Environ Sci 2016;9:1752–9.
[8] Xiao Z, Jia X, Ding L. Ternary organic solar cells offer 14% power conversion efficiency. Sci Bull 2017;62:1562–4.
[9] Guo W, Xu C, Zhu G, et al. Optical-fiber/TiO_2-nanowire-arrays hybrid structures with tubular counterelectrode for dye-sensitized solar cell. Nano Energy 2012;1:176–82.
[10] Hu G, Guo W, Yu R, et al. Enhanced performances of flexible ZnO/perovskite solar cells by piezo-phototronic effect. Nano Energy 2016;23:27–33.
[11] Zhang J, Tan CH, Du T, et al. ZnO-PCBM bilayers as electron transport layers in low-temperature processed perovskite solar cells. Sci Bull 2018;63:343–8.
[12] Zhu H, Fu Y, Meng F, et al. Lead halide perovskite nanowire lasers with low lasing thresholds and high quality factors. Nat Mater 2015;14:636–42.
[13] Tan ZK, Moghaddam RS, Lai ML, et al. Bright light-emitting diodes based on organometal halide perovskite. Nat Nanotechnol 2014;9:687–92.
[14] Xiao Z, Kerner RA, Zhao L, et al. Efficient perovskite light-emitting diodes featuring nanometre-sized crystallites. Nat Photon 2017;11:108–15.
[15] Feng J, Yan X, Liu Y, et al. Crystallographically aligned perovskite structures for high-performance polarization-sensitive photodetectors. Adv Mater 2017;29:1605993.
[16] Sichert JA, Tong Y, Mutz N, et al. Quantum size effect in organometal halide perovskite nanoplatelets. Nano Lett 2015;15:6521–7.
[17] Ling Y, Yuan Z, Tian Y, et al. Bright light-emitting diodes based on organometal halide perovskite nanoplatelets. Adv Mater 2016;28:305–11.
[18] Ha ST, Liu X, Zhang Q, et al. Synthesis of organic-inorganic lead halide perovskite nanoplatelets: towards high-performance perovskite solar cells and optoelectronic devices. Adv Opt Mater 2014;2:838–44.
[19] Zhang D, Eaton SW, Yu Y, et al. Solution-phase synthesis of cesium lead halide perovskite nanowires. J Am Chem Soc 2015;137:9230–3.
[20] Im JH, Lee CR, Lee JW, et al. 6.5% efficient perovskite quantum-dot-sensitized solar cell. Nanoscale 2011;3:4088–93.
[21] Wang Y, Li X, Song J, et al. All-inorganic colloidal perovskite quantum dots: a new class of lasing materials with favorable characteristics. Adv Mater 2015;27:7101–8.
[22] Huang H, Susha AS, Kershaw SV, et al. Control of emission color of high quantum yield $CH_3NH_3PbBr_3$ perovskite quantum dots by precipitation temperature. Adv Sci 2015;2:1500194.
[23] Huang S, Tang G, Huang H, et al. Enhanced piezo-response in copper halide perovskites based PVDF composite films. Sci Bull 2018;63:1254–9.
[24] Zhang Y, Xu W, Xu X, et al. Self-powered dual-color UV-green photodetectors based on SnO_2 millimeter wire and microwires/$CsPbBr_3$ particle heterojunctions. J Phys Chem Lett 2019;10:836–41.
[25] Deschler F, Price M, Pathak S, et al. High photoluminescence efficiency and optically pumped lasing in solution-processed mixed halide perovskite semiconductors. J Phys Chem Lett 2014;5:1421–6.
[26] Yang Y, Yan Y, Yang M, et al. Low surface recombination velocity in solution-grown $CH_3NH_3PbBr_3$ perovskite single crystal. Nat Commun 2015;6:7961.
[27] Zhang N, Sun WZ, Rodrigues SP, et al. Highly reproducible organometallic halide perovskite microdevices based on top-down lithography. Adv Mater 2017;29:160025.
[28] Zhang Q, Su R, Liu X, et al. High-quality whispering-gallery-mode lasing from cesium lead halide perovskite nanoplatelets. Adv Funct Mater 2016;26:6238–45.
[29] Jia Y, Kerner RA, Grede AJ, et al. Diode-pumped organo-lead halide perovskite lasing in a metal-clad distributed feedback resonator. Nano Lett 2016;16:4624–9.
[30] Liu Z, Yang J, Du J, et al. Robust subwavelength single-mode perovskite nanocuboid laser. ACS Nano 2018;12:5923–31.
[31] Wang X, Shoaib M, Wang X, et al. High-quality in-plane aligned $CsPbX_3$ perovskite nanowire lasers with composition-dependent strong exciton-photon coupling. ACS Nano 2018;12:6170–8.
[32] Li G, Che T, Ji X, et al. Record-low-threshold lasers based on atomically smooth triangular nanoplatelet perovskite. Adv Funct Mater 2019;29:180533.
[33] Zhang W, Peng L, Liu J, et al. Controlling the cavity structures of two-photon-pumped perovskite microlasers. Adv Mater 2016;28:4040–6.
[34] Zhou H, Yuan S, Wang X, et al. Vapor growth and tunable lasing of band gap engineered cesium lead halide perovskite micro/nanorods with triangular cross section. ACS Nano 2017;11:1189–95.
[35] Daniel W, Michael FD. Modeling crystal shapes of organic materials grown from solution. AIChE J 2000;46:1348–67.
[36] Chen Y, Yang S, Chen X, et al. Direct insight into crystallization and stability of hybrid perovskite $CH_3NH_3PbI_3$ via solvothermal synthesis. J Mater Chem A 2015;3:15854–7.
[37] Feng J, Yan X, Zhang Y, et al. "Liquid knife" to fabricate patterning single-crystalline perovskite microplates toward high-performance laser arrays. Adv Mater 2016;28:3732–41.
[38] D'Innocenzo V, Srimath Kandada AR, De Bastiani M, et al. Tuning the light emission properties by band gap engineering in hybrid lead halide perovskite. J Am Chem Soc 2014;136:17730–3.
[39] Liu Y, Zhang Y, Yang Z, et al. Multi-inch single-crystalline perovskite membrane for high-detectivity flexible photosensors. Nat Commun 2018;9:5302.
[40] Liu P, He X, Ren J, et al. Organic-inorganic hybrid perovskite nanowire laser arrays. ACS Nano 2017;11:5766–73.
[41] Eaton SW, Lai M, Gibson NA, et al. Lasing in robust cesium lead halide perovskite nanowires. Proc Natl Acad Sci USA 2016;113:1993–8.
[42] Manser JS, Kamat PV. Band filling with free charge carriers in organometal halide perovskites. Nat Photon 2014;8:737–43.
[43] Chen J, Fu Y, Samad L, et al. Vapor-phase epitaxial growth of aligned nanowire networks of cesium lead halide perovskites ($CsPbX_3$, X = Cl, Br, I). Nano Lett 2017;17:460–6.
[44] Zhang Q, Zhu X, Li Y, et al. Nanolaser arrays based on individual waved CdS nanoribbons. Laser Photon Rev 2016;10:458464.
[45] Zhang Q, Wang SW, Liu X, et al. Low threshold, single-mode laser based on individual cds nanoribbons in dielectric DBR microcavity. Nano Energy 2016;30:481–7.
[46] Justin C, Kelly P, Yan H, et al. Ultrafast carrier dynamics in single ZnO nanowire and nanoribbon lasers. Nano Lett 2004;4:197–204.

Fangtao Li is currently a Ph.D. candidate at School of Mathematics and Physics, University of Science and Technology Beijing. He has joined in the group of Professor Caofeng Pan at Beijing Institute of Nanoenergy and Nanosystems, Chinese Academy of Sciences as a visiting student since 2015. His research interests mainly focus on the synthesis of organic-inorganic hybrid perovskite and their application in photoelectric devices.

Caofeng Pan received his B.S. degree (2005) and Ph.D. degree (2010) in Materials Science and Engineering from Tsinghua University, China. He then joined the Georgia Institute of Technology as a postdoctoral fellow. He has been a professor and a group leader at Beijing Institute of Nanoenergy and Nanosystems, Chinese Academy of Sciences since 2013. His main research interests focus on the fields of piezotronics/piezo-photo tronics for new electronic and optoelectronic devices.

Anlian Pan received his Ph.D. from the Institute of Physics, Chinese Academy of Sciences in 2006. Afterwards, he worked one year as a Humboldt Research Fellow with Prof. Ulrich Goesele at the Max Planck Institute of Microstructure Physics, and then joined Arizona State University as a Postdoctoral Fellow, where he became a Research Assistant Professor. He came back to Hunan University and worked as the distinguished professor of "Furong" scholar in Hunan province in 2010. His research interests include the micro-nano optical, electronics of semiconductor nanostructures.

Tianfeng Li received his B.S. degree in physics at Henan University in 2001, and received his Ph.D. degree at Institute of Semiconductors, Chinese Academy of Sciences (CAS) under the supervision of Profs. Yonghai Chen and Zhanguo Wang in 2012. During 2015–2016, He worked as visiting scholar with Professor Caofeng Pan at Beijing Institute of Nanoenergy and Nanosystem, CAS. In 2012, he joined at the College of physics and electron at Henan University to start his independent career. His current research interests are focused on fabrication and optical property of nanomaterial.

Rongming Wang received his Bachelor and Master's Degrees in Physics from Peking University and Ph. D. in Materials Science from Beijing Institute of Aeronautical Materials, China. In 2004-2005, he was a visiting scholar in University of California, Berkeley. Then he joined Beihang University as a Professor in physics. Currently, he is a professor in University of Science and Technology Beijing, Director of Beijing Key Laboratory for Magneto-Photoelectrical Composite and Interface Science and Team Leader for Advanced Functional Material, Beijing Advanced Innovation Center of Materials Genome Engineering. His research interests include magnetic nanomaterial, transmission electron microscopy and interface science.